



The crucial role of hydroxyethyl methacrylate in the sintering of fused silica glass using ultraviolet-cured silica nanoparticle slurries: dispersing nanoparticles

Youwang Hu¹ · Guilin Wang¹ · Qinglong Zhang¹ · Xiaoyan Sun¹ · Haikuan Chen¹

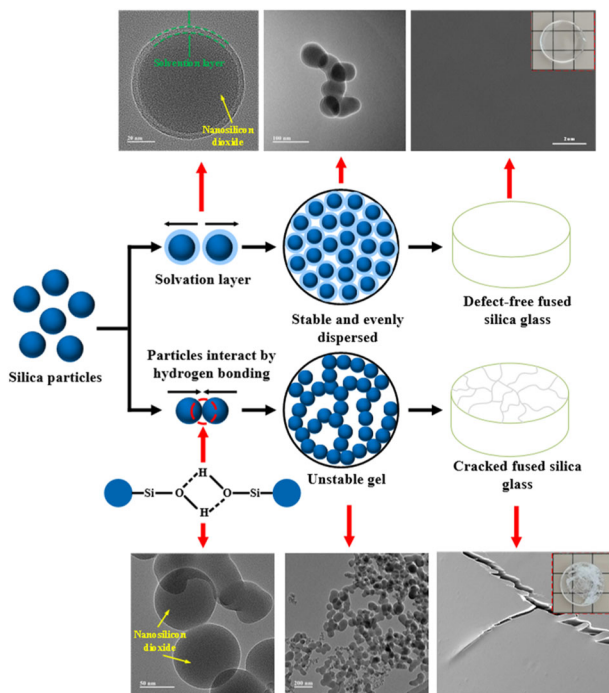
Received: 24 June 2024 / Accepted: 2 September 2024

© The Author(s), under exclusive licence to Springer Science+Business Media, LLC, part of Springer Nature 2024

Abstract

Fused silica glass is prepared by dispersing silica nanoparticles (SiNPs) through the hydroxyethyl methacrylate (HEMA). The dispersion of SiNPs was characterized using transmission electron microscopy and small angle X-ray scattering. The rheological properties and functional groups of SiNP slurries were analyzed utilizing a rotational rheometer and fourier transform infrared spectroscopy. The sintering quality of the fused silica glass was characterized through scanning electron microscopy and X-ray diffraction. The research results show that HEMA adsorbs on the surface of SiNP through hydrogen bonding to form a solvation layer of a certain thickness, thereby hindering the agglomeration of SiNPs. The SiNP slurry system exhibits bi-fractal properties. The viscosity and shear stress of the SiNP slurry initially decrease and then increase with increasing HEMA content. Achieving a homogeneous dispersion of SiNPs in the slurry is essential for sintering high-quality silica glass. The internal voids of agglomerates are the origin of crack formation.

Graphical Abstract



✉ Xiaoyan Sun
sunxy@csu.edu.cn

¹ State Key Laboratory of Precision Manufacturing for Extreme Service Performance, College of Mechanical and Electrical Engineering, Central South University, Changsha, China

Keywords HEMA · Hydrogen bonding · Silica nanoparticles · Solvation layer · Fused silica glass

Highlights

- The mechanism of dispersing silica nanoparticles by hydroxyethyl methacrylate (HEMA) was deeply investigated.
- The microstructure and rheological properties of silica nanoparticle slurries were analyzed.
- The effect of HEMA content on the sintering quality of fused silica glass was studied.
- The formation and origin of cracks during the sintering of fused silica glass were revealed.

1 Introduction

Fused silica glass is extensively applied in aerospace, inertial navigation and medical semiconductor industries owing to its corrosion resistance, high-temperature resistance, high hardness, chemical stability and electrical insulation [1–6]. However, fused silica glass parts with complex three-dimensional structures are difficult to manufacture [7] by conventional processes such as injection molding [8], grinding [9], plasma etching [10] and glass blowing [11]. This has largely limited the development of fused silica glass. The advent of light-curing 3D printing technology has brought enormous flexibility in the molding of fused silica glass. This technology has the advantages of short manufacturing cycles, the ability to machine complex models, reduced material waste, and gentle polymerization conditions [12]. Light-curing 3D printing technology requires the use of SiNP slurries as the “ink” for 3D printing, which are mainly composed of a mixture of SiNPs and curable resins [13]. For light-curing 3D printing, the adequate dispersion of SiNPs in curable resins is a crucial factor affecting the sintering quality of fused silica glass. Therefore, it is necessary to investigate the dispersion of SiNPs in curable resins.

Currently, there are two main methods to improve the dispersion of SiNPs. One method is to adjust the pH of the slurry. For example, Terpiłowski et al. [14] improved the dispersion of SiNPs in water/NaCl by adjusting the pH of silica slurry. However, adjusting the pH of the SiNP slurry introduces additional impurities that are detrimental to the sintering of high-quality fused silica glass. Another method is to modify the surface of SiNPs with small molecules or low molecular weight polymers. For example, the dispersion effect of SiNPs in suspension was improved by Zhang et al. [15] by creating a solvation layer on the SiNP surface using a combination of ethanol and water molecules. Chatterjee et al. [16] found that polyethylene glycol (PEG) molecules adsorbed on the silica particle surface through hydrogen bonding and formed a solvation layer to enhance the dispersion of SiNPs. Chen et al. [17] improved the dispersion of hydrophobic SiNPs in water by combining hydrophobic SiNPs with hydrophobic ends of cellulose nanofiber (CNF). The surface modification of SiNPs using 3-(Trimethoxysilyl) propyl methacrylate (KH570) improved the SiNPs dispersion stability by Tian et al. [18]. The ring-opening

reaction between epoxy groups of epoxidized solution-polymerized styrene–butadiene (ESSBR) and silanol groups on the SiNP surface was utilized by Yuan et al. [19] to successfully enhance the dispersion of SiNPs in ESSBR. However, ethanol/water, PEG and CNF do not possess C=C functional groups, and the molecular weight and viscosity of KH570 and ESSB are too high. Therefore, they are unsuitable for application as monomers or cross-linking agents for curable resins.

In contrast, HEMA is frequently employed as a monomer in curable resins because of its low viscosity, high dilution capability, and high reactivity [20]. In addition, the hydroxyl group at the end of the HEMA molecular chain has good dispersion for SiNPs. However, research on using HEMA dispersed silica nanoparticles to prepare fused silica glass lacks deep discussions of dispersion mechanisms, microscopic properties, rheological properties, sintering quality and cracking phenomena. To fill these gaps, this paper thoroughly investigates the mechanism of HEMA dispersed silica nanoparticles for the preparation of high-quality fused silica glass parts. The microstructure and rheological properties of SiNP slurries with different HEMA contents were analyzed. The effect of HEMA on the sintering quality of fused silica glass was clarified. Meanwhile, the formation and origin of cracks in the sintering process of fused silica glass were revealed. This study can provide theoretical guidance for the preparation of well-dispersed SiNP slurries and high-quality fused silica glass parts.

2 Materials and experimental methods

2.1 Materials

Aerosil OX50 amorphous silica nano-powder from Evonik, Germany, was used as the experimental material. Hydroxyethyl methacrylate (HEMA), polyethylene glycol diacrylate (PEGD), diethylene glycol di-benzoate (DEDB), and diphenyl (2,4,6-trimethylbenzoyl) phosphine oxide (TPO) were purchased from Shanghai Aladdin.

2.2 Preparation of SiNP slurry

The curable resin was made from a mixture of the monomer HEMA, the cross-linker PEGD, the plasticizer

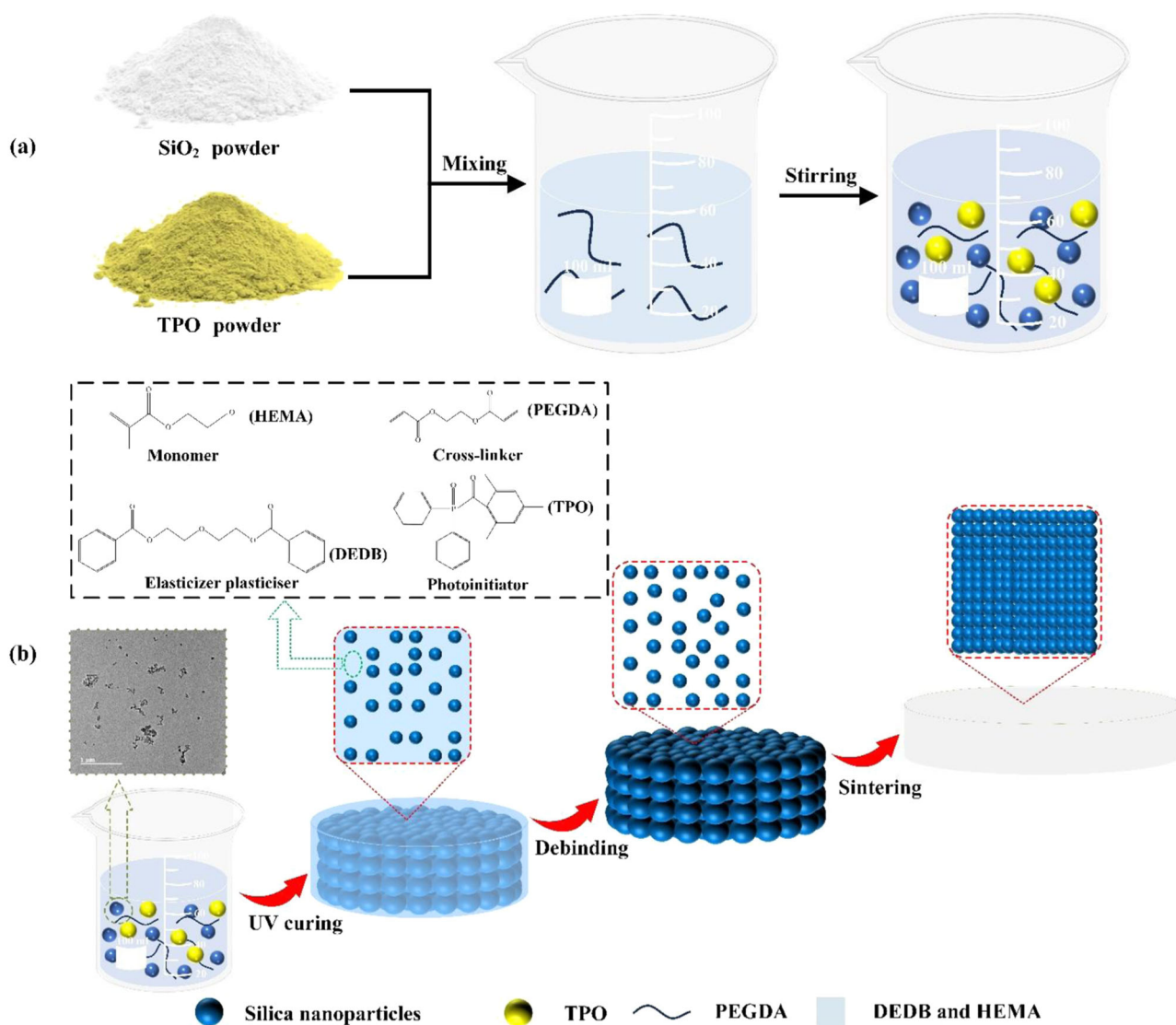


Fig. 1 Preparation of slurry (a) and fused silica glass (b)

DEDB and the photoinitiator TPO. The ratios of the light-curable resins were as follows: 15.45 wt% DEDB, 39.16 wt% PEGDA and HEMA, and 0.26 wt% TPO. HEMA and PEGDA were mixed in a ratio of $x/1-x$ ($x = 100 \text{ wt}\% \sim 50 \text{ wt}\%$). The 45 wt% amorphous silica powder was added to the configured light curable resin several times and stirred well, as shown in Fig. 1a. The prepared SiNP slurry was sonicated at 40 kHz for 20 min to eliminate air bubbles from the slurry.

2.3 Molding and heat treatment of green body

The configured slurry of silica nanoparticles was poured into a silicon rubber mold with a diameter of 33 mm and a height of 4 mm. Simultaneously, the molds were irradiated under a UV lamp with a power of 1000 W and a wavelength of 405 nm for 10 s for light-curing molding to form a green

body. The green body was put into the DZF-6020 vacuum drying oven (Changzhou Nuojie Instrument Co., Ltd., China) for drying treatment. The drying temperature was 60 °C, and the drying time was 12 h. Debinding of the green body was carried out using a KSL-1100X miniature box-type furnace (Hefei Kejing Material Technology Co., Ltd., China). During the debinding process, the heating rate was set at 0.5 °C/min until reaching 600 °C. The brown parts can be obtained without cracks by holding them at 90 °C, 253 °C, 338 °C, 500 °C, and 600 °C for 2 h, 4 h, 4 h, 4 h and 1 h, respectively. Then, the GSL-1600X high-temperature tube furnace was used for vacuum sintering. To achieve complete sealing of pores in the brown part, we increased the temperature to 1300 °C at a rate of 3 °C/min under a vacuum condition of 1×10^{-2} mbar. Transparent fused silica glass could be sintered under this condition, as shown in Fig. 1b.

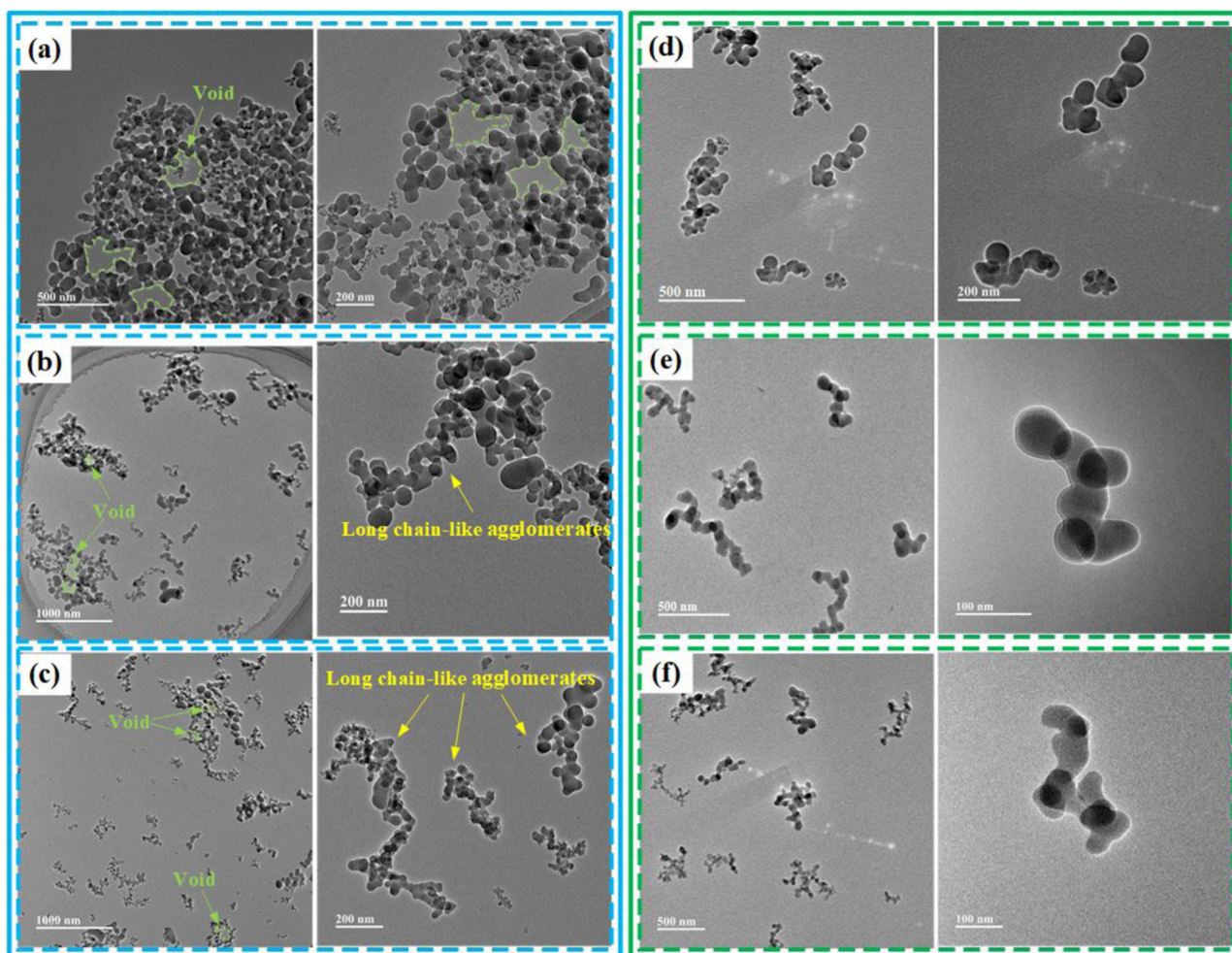


Fig. 2 Microstructure of SiNP slurries with HEMA contents of (a) HEMA = 50 wt%, b HEMA = 60 wt%, c HEMA = 70 wt%, d HEMA = 80 wt %, e HEMA = 90 wt%, f HEMA = 100 wt%

2.4 Microstructural characterization

The microstructure of the diluted SiNP slurry was observed with a JEOL F200 transmission electron microscope (JEOL Science and Technology Co., Ltd., Japan). A Xeuss 2.0 X-ray small angle scatterometer (Xenocs, France) was utilized for SAXS characterization. The functional groups in the SiNP slurry were analyzed using an IRTracer 100 fourier transform infrared spectroscopy instrument manufactured by Shimadzu in Japan. Fourier transform infrared spectroscopy experiments were conducted using the KBr disk method. Rheological properties were performed utilizing an MCR 302 rotational rheometer (Anton Paar, Austria). Thermogravimetry analysis was performed employing a STA2500 regular thermal analyzer (Netzsch, Germany). The physical phases were analyzed through UltimaIV X-ray diffraction (Rigaku, Japan). The copper target was used for the experiment. The scanning step was 5°/min and the diffraction angle was varied from 10° to 90°. The surface morphology of the samples was observed using a

Tescan Mira4 field emission scanning electron microscope (Tescan, Czech Republic).

3 Results and discussion

3.1 Microstructure of SiNP slurry

The microstructure of SiNP slurries with different HEMA contents is shown in Fig. 2. When HEMA = 50 wt%, SiNPs aggregated in the curable resin to form network-like microstructures. A 100–500 nm void appeared inside the network after the gel network was formed by the aggregation of multiple agglomerates, as shown in Fig. 2a. When the content of HEMA was increased, the gel network structure was gradually opened to form long chain-like agglomerates with loose structures (Fig. 2b, c). Voids were also present inside long chain-like agglomerates. With the further increase of HEMA content to more than 70 wt%, the long-chain SiNP agglomerates gradually

Fig. 3 2D SAXS images of SiNP slurries with different HEMA contents

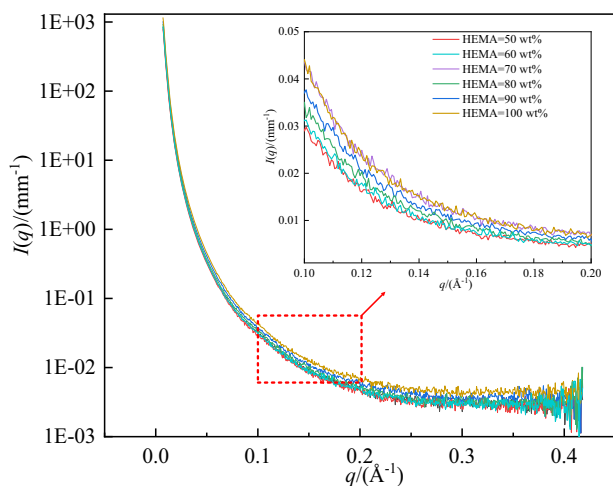
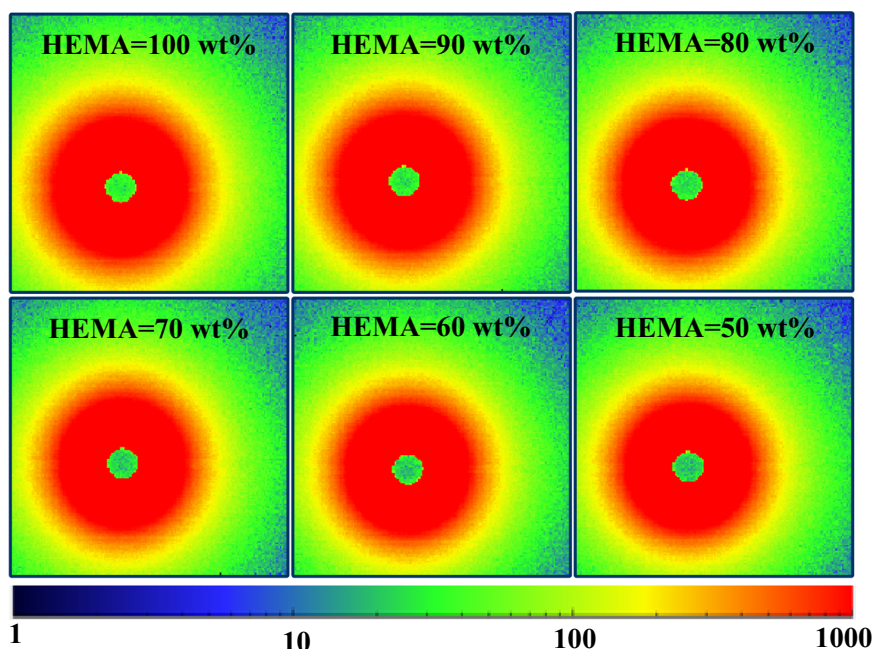


Fig. 4 $I(q)$ – q curves

disappeared to form stable nanoscale short chain-like agglomerates, as shown in Fig. 2d–f. At this time, the SiNP slurry was also transformed from a gel state to a sol. The above results indicate that HEMA can effectively hinder the accumulation of SiNPs.

In addition, we used SAXS to analyze the internal structure of the SiNP slurry with 2D SAXS images obtained, as shown in Fig. 3. From Fig. 3, the 2D SAXS images all show circles of uniform size, which implies that the SiNP slurries were isotropic. Therefore, the physical properties of the SiNP slurry do not change with the measurement direction.

Figure 4 shows the $I(q)$ – q curves. when $q < 0.05$, $I(q)$ decreased rapidly. However, the $I(q)$ change gradually

decreases as q increases. It is worth noting that the $I(q)$ – q curves of SiNP slurries with different HEMA contents are slightly different. The $I(q)$ – q curve gradually raised with increasing HEMA content. It shows that HEMA has a better dispersion for SiNPs. The lowest $I(q)$ – q curve was observed when the HEMA = 50 wt%, which indicated that the SiNP agglomerates had the largest particle size. The SAXS test results agree with those of the TEM microscopic results.

Figure 5 shows the $[\ln I(q)] - \ln(q)$ curves that can be obtained from the $I(q)$ – q curves. The information about the homogeneity of the agglomerates can be obtained by fractal analysis of the $[\ln I(q)] - \ln(q)$ curves. When $1 < -d < 3$, then the slope d of the $[\ln I(q)] - \ln(q)$ curve can be fractal analyzed. This fractal is a mass fractal, which shows that the mass M of the agglomerate changes exponentially with its radius R .

$$M \propto R^{D_m} \quad (1)$$

$$D_m = -d \quad (2)$$

Where, D_m is the mass fractal, reflecting information such as the aggregation state.

When $3 < -d < 4$, the surface fractal can be analyzed according to Eq. (3).

$$D_s = 6 + d \quad (3)$$

Where, D_s is the surface fractal dimension, which can effectively reflect the irregularity of the particle surface. The smaller the D_s value, the smoother the agglomerate surface. The particles are dense and smooth at $D_s = 2$.

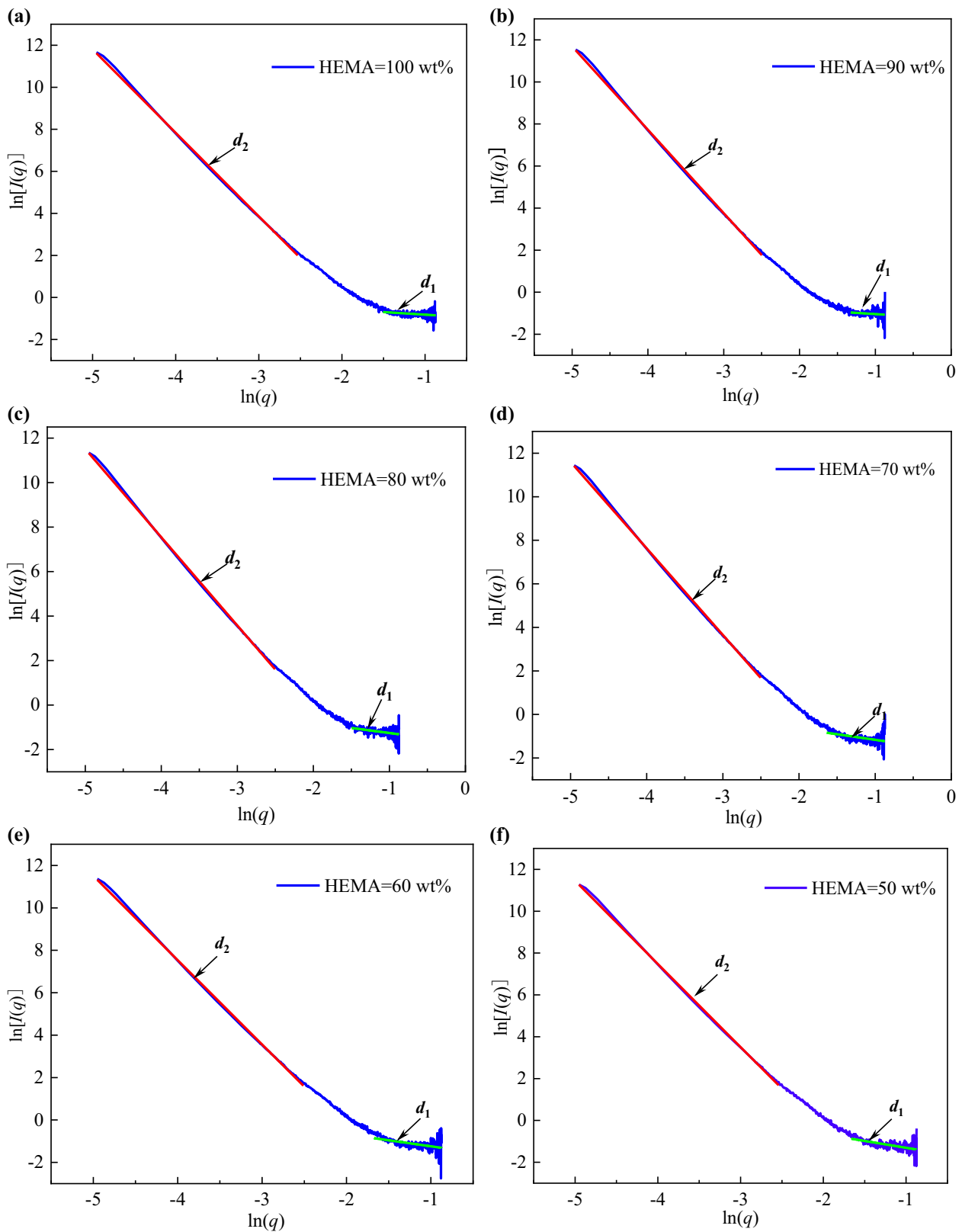


Fig. 5 $\ln[I(q)] - \ln(q)$ curve. The slope is denoted as d_1 when $-1 < \ln(q) < -1.5$ and d_2 when $-2.5 < \ln(q) < -5$. **a** HEMA = 100 wt%, **b** HEMA = 90 wt%, **c** HEMA = 80 wt%, **d** HEMA = 70 wt%, **e** HEMA = 60 wt%, **f** HEMA = 50 wt%

Table 1 Results of fractal analysis

HEMA	100 wt%		90 wt%		80 wt%		70 wt%		60 wt%		50 wt%	
	d_1	d_2	d_1	d_2	d_1	d_2	d_1	d_2	d_1	d_2	d_1	d_2
Slope												
	-0.2467	-3.973	-0.2261	-3.965	-0.4542	-3.967	-0.5101	-3.974	-0.5684	-3.976	-0.6510	-3.984
Fractal information	D_m	D_s	D_m	D_s	D_m	D_s	D_m	D_s	D_m	D_s	D_m	D_s
	0.2467	2.027	0.2261	2.035	0.4542	2.033	0.5101	2.026	0.5684	2.024	0.6510	2.016

Figure 5 shows the double logarithmic curves of the SiNP slurry fractal properties. When $-1 < \ln(q) < -1.5$, the curve had a linear portion with the slope noted as d_1 . The curve also appears linear for $-2.5 < \ln(q) < -5$, where the slope was noted as d_2 . Two linear regions, d_1 and d_2 , correspond to the mass fractal and surface fractal, respectively. This phenomenon demonstrates the presence of bi-fractal properties in the system. The distribution and agglomeration of SiNPs in the system is a stochastic and nonlinear process, which also predicts the presence of an interfacial phase.

Table 1 shows the fractal results of the SiNP slurries obtained according to Fig. 5. From Table 1, the D_m exhibited a decreasing trend as the HEMA content increased from 50 wt% to 90 wt%. The D_m reached a minimum value when HEMA content is 90 wt%. The mass fractal results show that the mass distribution of the gel network formed by aggregation of SiNPs becomes inhomogeneous with the HEMA increase. Also, the network structure of the gel gradually becomes looser as HEMA increases. The slurry was transformed from a gel to a sol. This phenomenon may be due to the gradual decrease in the size of SiNP agglomerates and the increase in the thickness of the interface layer under the action of HEMA. The increase in the thickness of the interface layer erodes SiNPs with the closely distributed mass, resulting in the gel network structure becoming loose [21]. However, the D_m value increased instead with a further increase in HEMA content. Excessive HEMA incorporation leads to a bridging effect between the interface layers on the SiNP surface. This bridging effect will somewhat exacerbate the SiNP aggregation [22], increasing the D_m value.

When the HEMA content was increased from 50 wt% to 90 wt%, the surface fractal D_s values also increased gradually, and the D_s were all greater than 2, as shown in Table 1. The increase in D_s value may be attributed to the fact that the number of HEMA molecules anchored to the SiNP surface increases with HEMA content, resulting in a rougher surface. Whereas, the fractal surface D_s value decreases to 2.027 when the content of HEMA reaches 100 wt%. The phenomenon occurs because the HEMA molecules adsorbed on the surface of the SiNPs reach their limit. A uniform solvation layer is formed on the SiNP surface, decreasing in the D_s value.

Porod theory can be used to analyze the structure of sol-gel interfaces. According to Porod's theory, when the system is composed of two phases with a sharp interface, the curve $[q^3 I(q)] - q^2$ tends to be a straight line when under the

condition of the scattering angle is significant, as shown by the curve A in Fig. 6a.

$$\lim_{q \rightarrow \infty} [q^3 I(q)] = K \quad (4)$$

However, in many cases, the systems we study are not ideal two-phase systems. On the contrary, when q tends to large values, $q^3 I(q)$ is not a constant and the curves show positive and negative deviations, as shown in curves B and C in Fig. 6a. Positive deviations are caused by factors such as the heat density in the material and the electron density inhomogeneity within the particles. Now, the curve $[q^3 I(q)] - q^2$ is formulated as follows:

$$I(q) = Kq^{-3} \exp(\sigma^2 q^2) \quad (5)$$

The generation of negative deviation is attributed to the unclear phase boundary. This means there is no clear phase boundary between the two phases, and a transition region of a certain width exists between them (i.e., interfacial layer or dissolution layer). Now, the $[q^3 I(q)] - q^2$ curve exhibits a negative deviation in the high angle region.

$$I(q) = Kq^{-3} \exp(-\sigma^2 q^2) \quad (6)$$

From Fig. 6b, the slope at the end of the $[q^3 I(q)] - q^2$ curve was negative when the HEMA content was 80 wt% to 100 wt%. It indicates that the system does not obey Porod's theorem, where different degrees of negative deviation are present. Meanwhile, it also shows the presence of interface layers in the system [23]. The slope at the end of the $[q^3 I(q)] - q^2$ curve changes from negative to positive as the HEMA content decreases, i.e., there was a positive deviation of the $[q^3 I(q)] - q^2$ curve, as shown in the inset in Fig. 6b. The inhomogeneous heat and electron densities in the system lead to a positive deviation of the $[q^3 I(q)] - q^2$ curve. It shows that when the HEMA content is lower than 70 wt%, the SiNPs start to exhibit some degree of agglomeration.

3.2 Rheological properties and FT-IR analysis

Figure 7 shows the viscosity of SiNP slurries with different HEMA contents. Figure 7 was divided into two areas, I and II,

corresponding to shear rates of $0\text{--}20\text{ s}^{-1}$ (low shear rate area) and $20\text{--}100\text{ s}^{-1}$ (high shear rate area), respectively. In area I, the viscosity decreases as the shear rate increases. The slurry had a shear-thinning behavior. In area II, the viscosity increases with the shear rate. The slurry showed shear thickening behavior. The shear behavior of areas I and II has been analyzed as follows. In the initial state, the arrangement of SiNPs in the slurry is

disordered and the network structure is formed [24], as shown in Fig. 8a. These network structures are difficult to move. Consequently, the slurry exhibits a higher viscosity. The network structure is opened as the shear rate increases. The SiNPs formed an ordered arrangement under the shear force, as shown in Fig. 8b. Relative motion between SiNPs is more likely to occur. So, the macroscopic manifestation is a reduction in the viscosity of the slurry. When the shear rate is increased to area II, the fluid lubrication force of the slurry destroys the short-range friction between the SiNPs [25]. The SiNPs form agglomerates (Fig. 8c), so the slurry exhibits shear thickening at high shear rates [26].

Calculate the average viscosity in the shear rate range of $0\text{--}10^2\text{ s}^{-1}$, as shown in Fig. 9. From Fig. 9, the viscosity of the slurry was reduced by 2.665%, 41.864%, 6.866%, and 41.35% as HEMA content increased from 50 wt% to 90 wt%. The

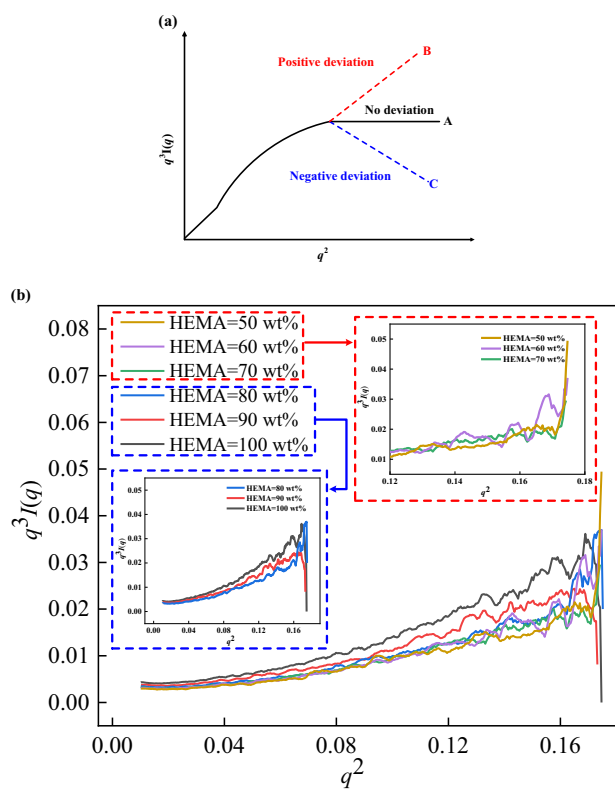


Fig. 6 Porod curves of SiNPs. **a** Porod theory and its deviations. **b** $[q^3 I(q)]\text{--}q^2$ curves

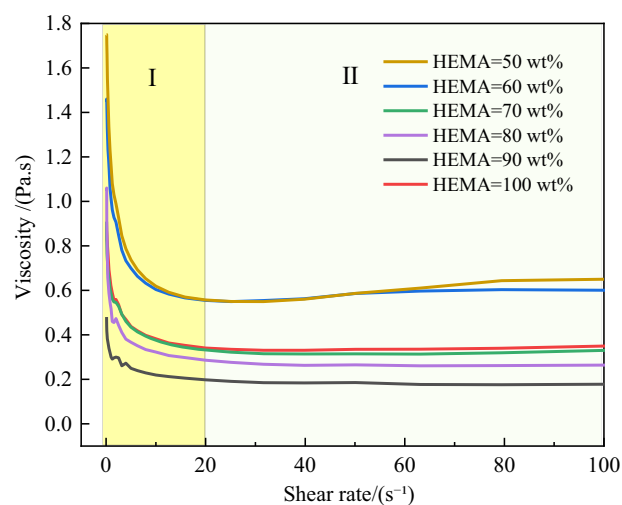


Fig. 7 The viscosity of SiNP slurries with different HEMA contents

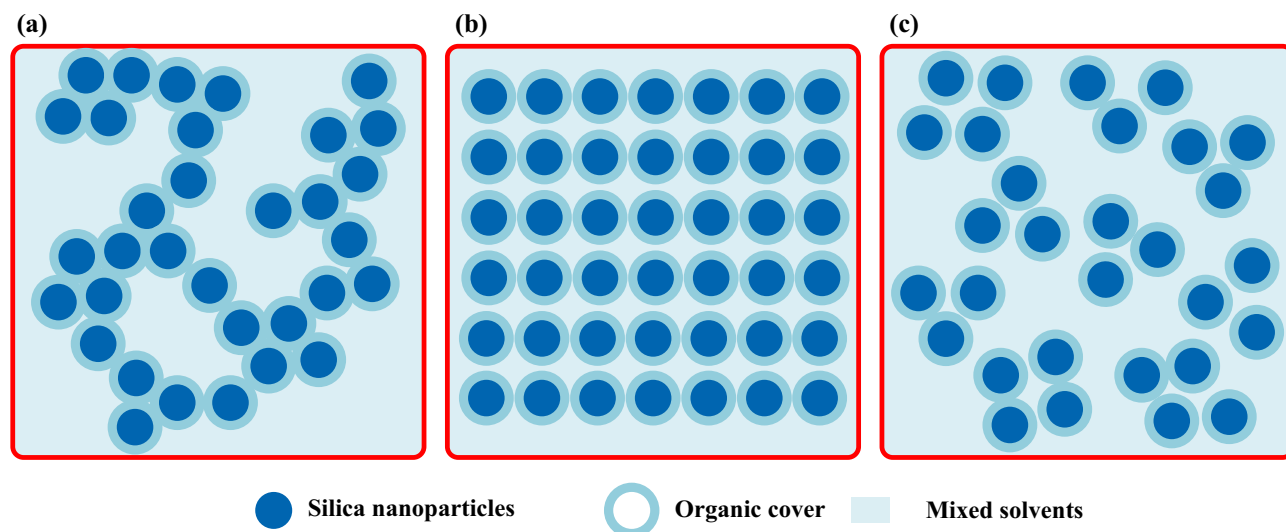


Fig. 8 Shear rheological properties of slurry. **a** static state, **b** low shear rates, **c** high shear rate

viscosity of the SiNP slurry decreased from 0.9910 to 0.2821 Pa.s. Interestingly, the viscosity of the slurry exhibited a significant increase when HEMA was further added, reaching a value of 0.5401 Pa.s. The minimum viscosity of the slurry was obtained when the HEMA content was 90 wt%, as shown in

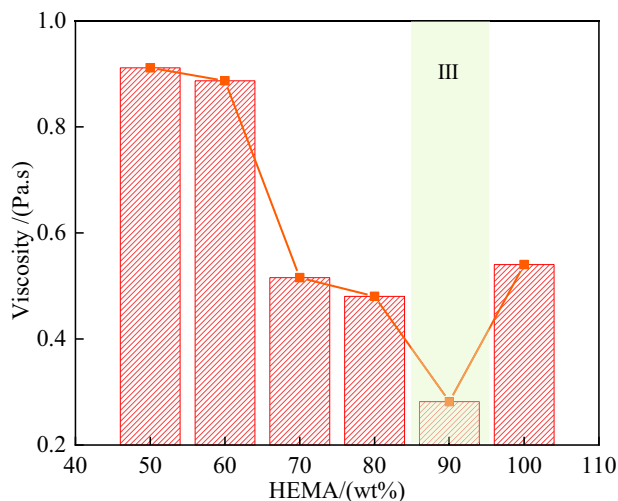


Fig. 9 Average viscosity of slurries with different HEMA contents

area III in Fig. 9. We also measured the average shear stress of the slurry, as shown in Fig. 10. As HEMA content increased from 50 wt% to 90 wt%, the shear stress of the slurry was reduced by 41.05%, 44.18%, 16.58%, and 31.91% (from 15.99 Pa to 2.988 Pa), respectively. The slurry shear stress

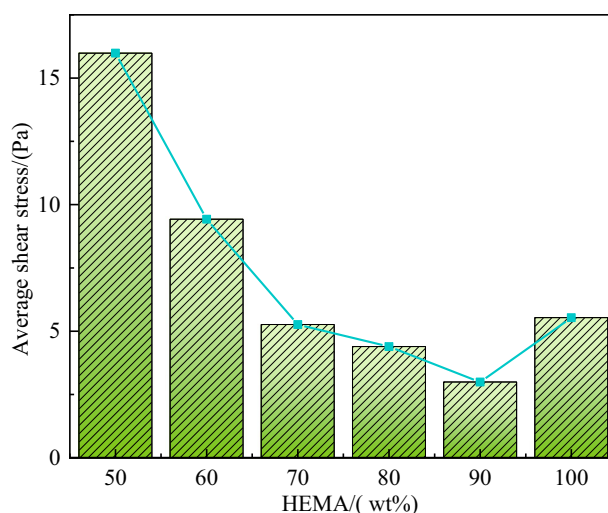


Fig. 10 Average shear stress of slurries with different HEMA contents

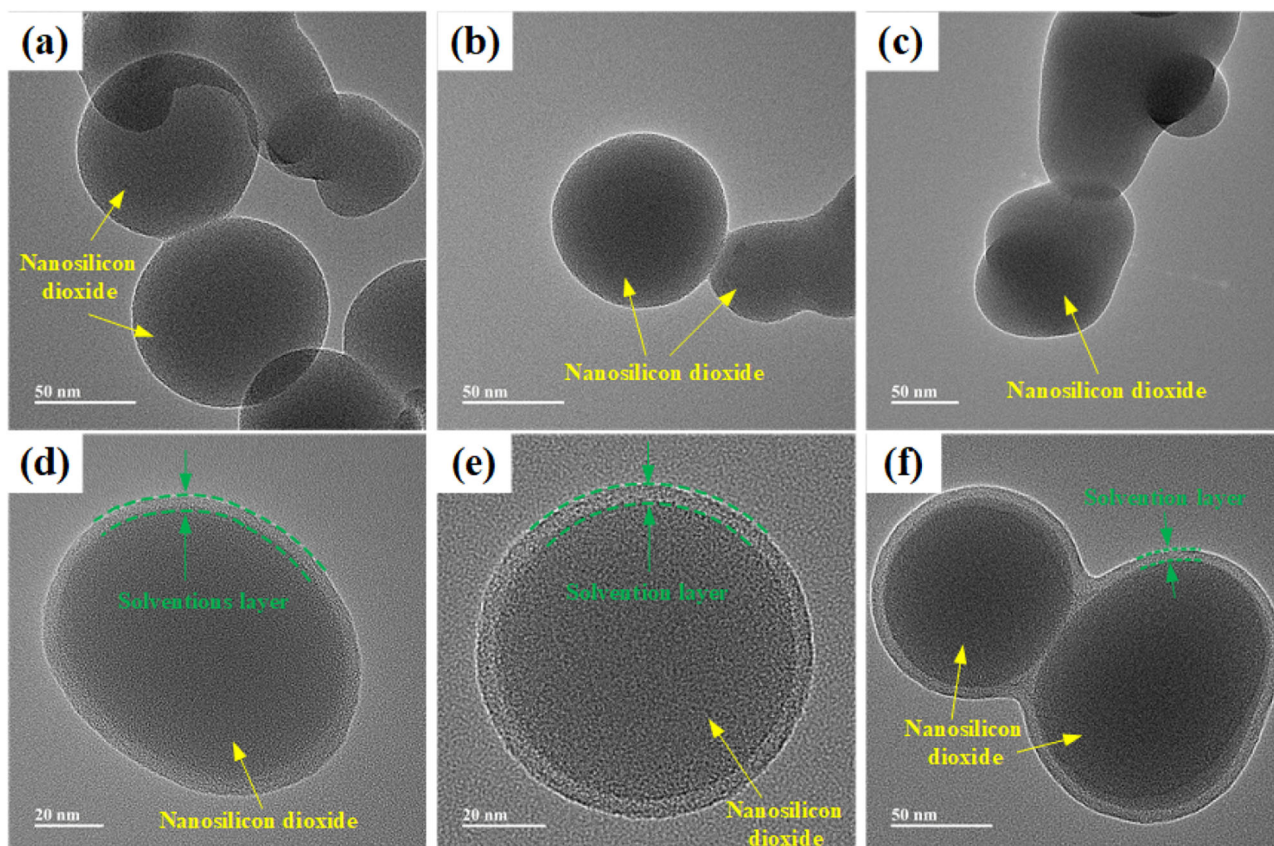


Fig. 11 The solvation layer on the silica nanoparticle surface at different HEMA contents. **a** HEMA = 50 wt%, **b** HEMA = 60 wt%, **c** HEMA = 70 wt%, **d** HEMA = 80 wt%, **e** HEMA = 90 wt%, **f** HEMA = 100 wt%

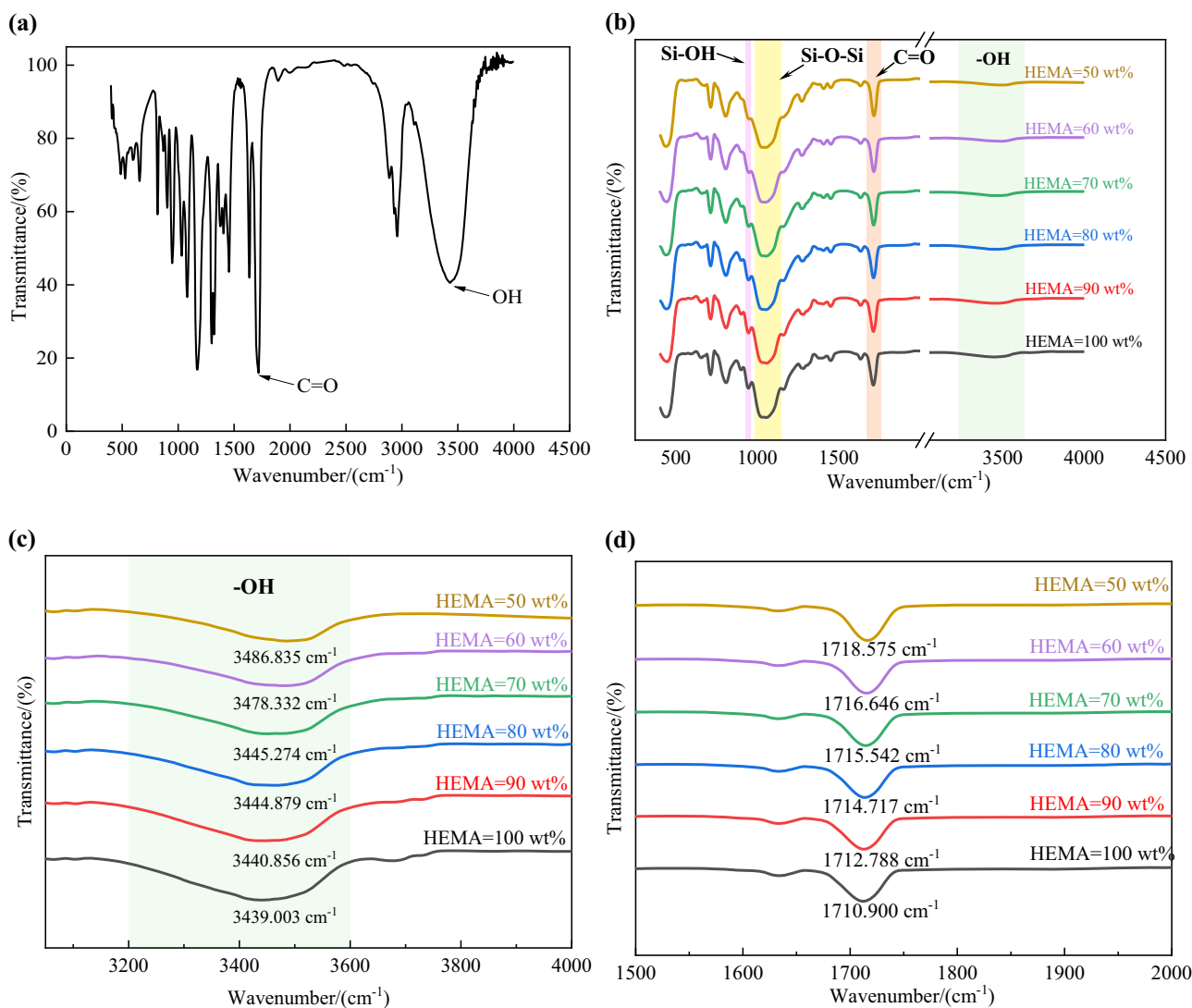


Fig. 12 FT-IR spectra of SiNP slurries and HEMA. **a** FT-IR spectra of HEMA. **b** FT-IR spectra of slurries. **c** Enlarged view of FT-IR spectrum of hydroxyl group. **d** Enlarged view of FT-IR spectrum of C=O

increased to 5.532 Pa instead when the HEMA content was increased to 100 wt%. The trend of shear stress variation with HEMA content was consistent with viscosity. The above experimental results show that HEMA can effectively reduce the viscosity and shear stress of SiNP slurry. Shear stress and viscosity decrease and then increase with increasing HEMA content, achieving a minimum at HEMA = 90 wt%.

To further analyze the reasons for the change in the slurry rheological properties, we directly observed the SiNP surface at higher magnification using a TEM, as shown in Fig. 11. We did not observe a solvation layer on the SiNP surface when HEMA \leq 70 wt%. Agglomerates were formed by direct contact between SiNPs (Fig. 11a–c). The slurry exhibits high viscosity and high shear stress owing to the poor flowability of the agglomerates. From Fig. 11d, e, the SiNPs were fully dispersed, and a solvation layer with a thickness of 3–5 nm was clearly observed on the

particle surface with the increase of HEMA content. Due to the steric hindrance mechanism, SiNPs maintain stable dispersion in the slurry [27], which greatly improves the fluidity of the slurry. So, the viscosity and shear stress of the slurry decreased gradually as HEMA content increased. When the content of HEMA was further increased up to 100 wt%, we observed an overlapping of the solvation layers, interpenetrating each other, and the SiNPs were close to each other, as shown in Fig. 11f. This phenomenon indicates that the bridging effect between particles begins to occur [22]. The bridging effect accelerates the aggregation of the powder to some extent, thereby increasing the viscosity and shear stress of the slurry [28]. The experimental results above indicate that HEMA hinders the agglomeration of SiNPs by adsorbing on the SiNP surface to form a solvation layer. Additionally, HEMA improves the flowability of the slurry, but the amount of HEMA added exhibits a threshold.

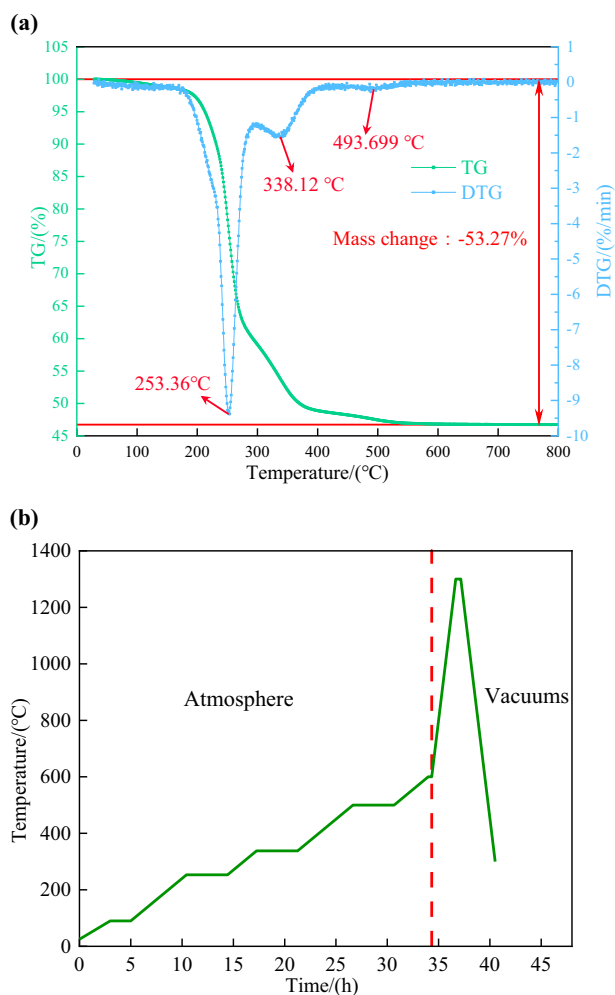


Fig. 13 TG–DTG curve and heat treatment process. **a** TG–DTG curve. **b** Temperature rise curve

We performed FT-IR spectroscopy on the slurry to further explain the mechanism of HEMA dispersed silica nanoparticles. The stretching vibrations of the C=O and hydroxyl group of HEMA were observed at 1720 cm^{-1} and $3200\text{--}3600\text{ cm}^{-1}$, respectively, as shown in Fig. 12a. Figure 12b shows the FT-IR spectrum of the SiNP slurry. The Si-O-Si stretching vibration appears as broadband at $1000\text{--}1150\text{ cm}^{-1}$ [29]. The absorption peak at 951.0 cm^{-1} corresponds to the Si-OH [30]. The IR spectra of the hydroxyl group and C=O of SiNP slurries were magnified, as shown in Fig. 12c, d. From Fig. 12c, d, the absorption peak of the hydroxyl group at 3486 cm^{-1} shifted to 3439 cm^{-1} , and the C=O peak shifted from 1718 cm^{-1} to 1710 cm^{-1} with increasing HEMA content [31–33]. Additionally, the absorption peak of the Si-OH shifted from 951.0 cm^{-1} to 945.2 cm^{-1} . These shifts indicate the formation of hydrogen bonds between the hydroxyl and carbonyl groups of HEMA and the silanol groups on the SiNP surface [34–36]. Based on the above experiments, we can infer that HEMA is adsorbed on the SiNP surface through hydrogen bonding to form a solvation layer.

3.3 Heat treatment and microstructure analysis

Thermogravimetry analysis of the green body was conducted, as shown in Fig. 13a. Analysis of the DTG and TG curves showed significant mass loss of the green body at $253.4\text{ }^{\circ}\text{C}$, $338.7\text{ }^{\circ}\text{C}$ and $493.7\text{ }^{\circ}\text{C}$. The DTG curve levels off after reaching $500\text{ }^{\circ}\text{C}$, indicating that the thermal decomposition of organic compounds in the green body is essentially completed. After the debinding process was completed, the mass loss of the green body was 53.28% . Thus, the debinding temperatures were set at $253.4\text{ }^{\circ}\text{C}$, $338.7\text{ }^{\circ}\text{C}$, and $493.7\text{ }^{\circ}\text{C}$ to remove organic compounds altogether. Additionally, a holding step was introduced during the debinding process to ensure the complete decomposition of organic compounds within that temperature range. We adjusted the debinding process based on preliminary experiments, as shown in Fig. 13b. During the debinding process, the heating rate was set at $0.5\text{ }^{\circ}\text{C}/\text{min}$ until reaching $600\text{ }^{\circ}\text{C}$. The brown parts can be obtained without cracks by holding them at $90\text{ }^{\circ}\text{C}$, $253\text{ }^{\circ}\text{C}$, $338\text{ }^{\circ}\text{C}$, $500\text{ }^{\circ}\text{C}$ and $600\text{ }^{\circ}\text{C}$ for 2 h, 4 h, 4 h, 4 h and 1 h, respectively. To achieve complete sealing of pores in the brown part, we increased the temperature to $1300\text{ }^{\circ}\text{C}$ at a rate of $3\text{ }^{\circ}\text{C}/\text{min}$ under a vacuum condition of 1×10^{-2} mbar. Subsequently, the temperature was maintained for 30 min to complete the densification process of the fused silica glass.

Figure 14 shows the optical and SEM images of the brown parts at different HEMA contents after sintering at $1300\text{ }^{\circ}\text{C}$ for 30 min, showing different features. When the HEMA content ranged from 80 wt% to 100 wt%, the brown part sintering was more effective, and transparent and dense fused silica glass was obtained with smooth surfaces and free of any defects, as shown in Fig. 14a–c. However, when the HEMA content was lower than 70 wt%, surface defects, such as cracks, were observed on the fused silica glass after sintering, as shown in Fig. 14d–f. Also, we performed X-ray diffraction (XRD) physical phase analysis on the fused silica glass in Fig. 14, as shown in Fig. 15. The X-ray diffraction peaks show a humping, indicating that the sintered product is amorphous fused silica glass with no crystallization behavior.

HEMA adsorbs on the surface of the SiNPs through hydrogen bonding to form a solvation layer at high HEMA content ($>70\text{ wt}\%$). Under the effect of the steric hindrance mechanism, when SiNPs are close to each other, the solvation layer on their surface is compressed, which triggers repulsive forces and prevents direct contact and agglomeration between particles. So, the silica nanoparticles are uniformly, stably and orderly dispersed in the slurry. The adequately dispersed slurry was light-cured to form a green body, which a defect-free, transparent and dense fused silica glass was obtained after sintering, as shown in Fig. 16a. However, when the

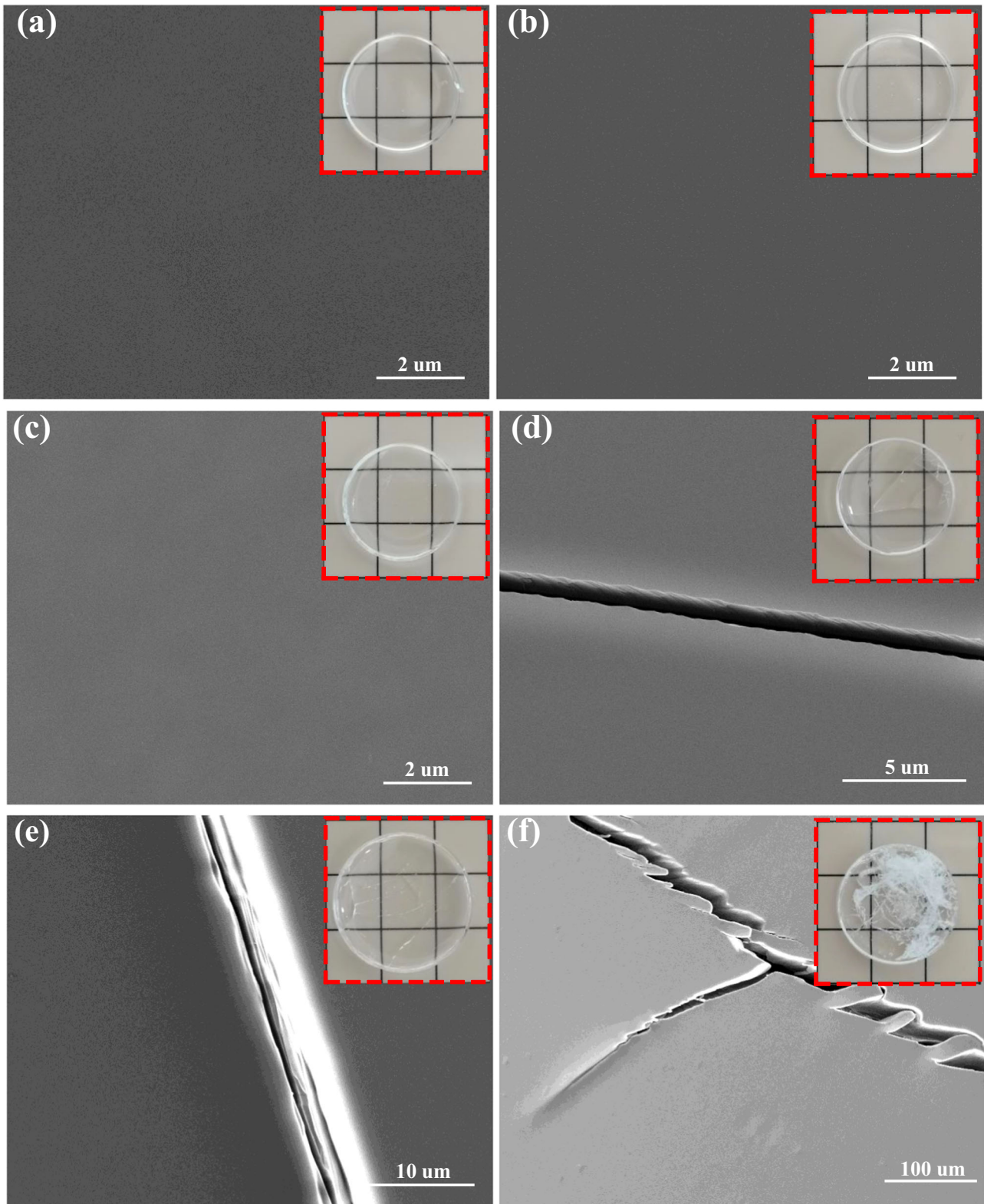


Fig. 14 Optical and SEM images of brown parts with different HEMA contents after sintering at 1300 °C for 30 min. **a** HEMA = 100 wt%, **b** HEMA = 90 wt%, **c** HEMA = 80 wt%, **d** HEMA = 70 wt%, **e** HEMA = 60 wt% and **f** HEMA = 50 wt%

HEMA content was not sufficient to coat the SiNPs (HEMA ≤ 70 wt%), hydrogen bonds were formed between the different SiNPs through the silanol groups on the surface, which agglomerated together to form agglomerates [37]. Multiple agglomerates aggregated to form the gel network and long chain-like agglomerates, which have many internal voids, as shown in Fig. 2a–c. The internal voids formed by agglomerate aggregation are the weak areas of the light-cured green body. During

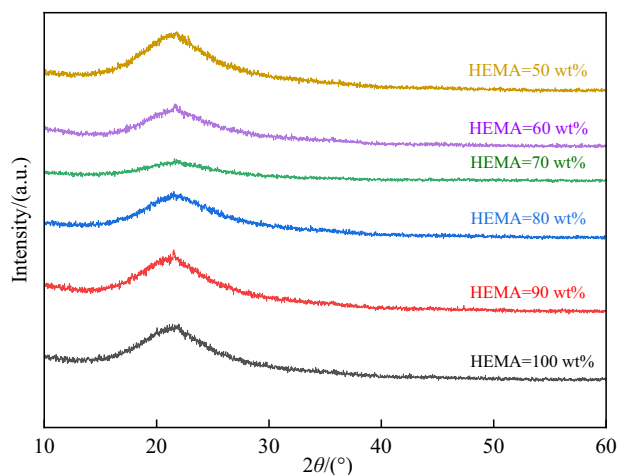


Fig. 15 X-ray diffraction analysis of sintered fused silica glass at 1300 °C

the debinding process, the resin filling the voids in the green body undergoes thermal decomposition to form cracks, which is the origin of crack formation [38]. Concurrently, at high-temperature sintering, the brown part shrinkage generates large shrinkage and thermal stresses [39, 40]. Shrinkage and thermal stresses caused the cracks to further enlarge and extend, as shown in Fig. 16b.

From Sections 3.1 and 3.2, the bridging between the solvation layers on the surfaces of different SiNPs occurred when the HEMA content reached 100 wt%, which led to a certain degree of agglomeration of the SiNPs. However, this agglomeration phenomenon is not very serious and the formed agglomerates still exhibit stable nanoscale short chain-like structures, as shown in Fig. 2f. So, when the HEMA content reached 100 wt%, the sintered fused silica glass also did not show defects such as cracks.

4 Conclusions

In this study, the microstructure and rheological properties of SiNP slurries were analyzed, and the mechanism of dispersing SiNPs by HEMA was deeply investigated. The sintering quality of fused silica glass was studied by analyzing the surface topography and physical phase of fused silica glass. The formation and origin of cracks during the sintering of fused

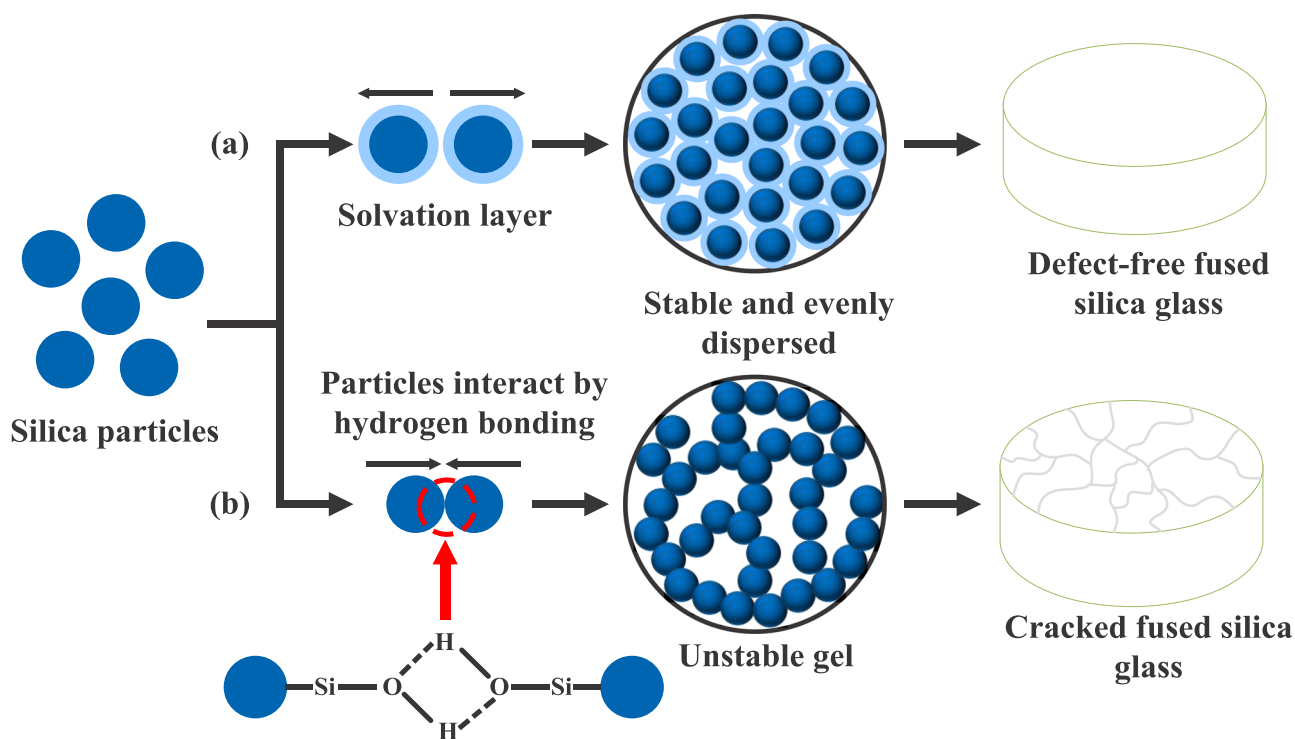


Fig. 16 Dispersion evolution of silica nanoparticles in a curable resins and sintering [41, 42]. **a** Dispersion mechanism and sintering process of silica nanoparticles in curing resins. **b** Silicon dioxide nanoparticle agglomeration in curable resins and crack generation during sintering

silica glass were revealed by the dispersion evolution of SiNPs in curable resins. The several critical conclusions were drawn:

1. HEMA can effectively disperse silica nanoparticles. As the content of HEMA increases, gel networks and long chain-like agglomerates are dispersed into stable nanoscale short chain-like structures.
2. The SiNP slurry system exhibits mass fractal and surface fractal properties, in which the distribution and agglomeration of particles is a random and nonlinear process. With the HEMA content, the mass fractal trend decreases and then increases, while the surface fractal changes by first increasing and then decreasing.
3. The shear stress and viscosity of the slurry first decrease and then increase with the HEMA content. HEMA adsorbs on the SiNP surface to form a solvation layer of a certain thickness for dispersing SiNPs.
4. Defect-free fused silica glass can be prepared when the HEMA content is 80 wt%–100 wt%. When the HEMA content is below 70 wt%, the fused silica glass obtained by sintering shows defects such as cracks. Crack formation originates from voids within the gel network and long chain-like aggregates. Shrinkage and thermal stresses generated during the sintering process can cause cracks to further enlarge and extend.

Acknowledgements This work was supported by the National Natural Science Foundation of China (51935013, 51875585, and 51875584).

Author contributions Youwang Hu: Writing—review & editing, Resources, Supervision; Guilin Wang: Investigation, Formal analysis, Visualization, Writing—original draft; Qinglong Zhang: Conceptualization, Supervision; Xiaoyan Sun: Methodology, Supervision; Haikuan Chen: Visualization.

Compliance with ethical standards

Conflict of interest The authors declare no competing interests.

References

1. Wang Z, Wang P, Dong F, Pang M, Ma L, Zhao H, Su J (2024) Performance on lapping quartz glass by UV curing fixed abrasive pad with Gr₂O₃-diamond composite abrasives. *Mater Sci Semicond Process* 169:107926. <https://doi.org/10.1016/j.mssp.2023.107926>
2. Blaineau P, André D, Laheurte R, Darnis P, Darbois N, Cahuc O, Neauport J (2015) Subsurface mechanical damage during bound abrasive grinding of fused silica glass. *Appl Surf Sci* 353:764–773. <https://doi.org/10.1016/j.apsusc.2015.07.047>
3. Liu Y, Tong H, Li Y, Che J (2023) The effect of tool wear on the damaged layer thickness and tool wear rate in ultra-precision turning of quartz glass. *J Micromech Microeng* 33(9):095012. <https://doi.org/10.1088/1361-6439/acea8b>
4. Shetty S, Mishra DK, Dixit P, Shetty SS, Jayarama AA Shah P (2023) Etching of micro-channels in fused quartz for novel device applications. *Mater Today Proc.* <https://doi.org/10.1016/j.matpr.2023.07.253>
5. Zhao Z, Zhang Z, Shi C, Feng J, Zhuang X, Li L, Meng F, Li H, Xue Z, Liu D (2023) Dispersion and polishing mechanism of a novel CeO₂-LaOF-based chemical mechanical polishing slurry for quartz glass. *Mater* 16(3):1148. <https://doi.org/10.3390/ma16031148>
6. Lin B, Li S, Cao ZC, Zhang Y, Jiang XM (2021) Theoretical modeling and experimental analysis of single-grain scratching mechanism of fused quartz glass. *J Mater Process Technol* 293:117090. <https://doi.org/10.1016/j.jmatprotec.2021.117090>
7. Bauer J, Crook C, Baldacchini T (2023) A sinterless, low-temperature route to 3D print nanoscale optical-grade glass. *Science* 380:960–966. <https://doi.org/10.1126/science.abq3037>
8. Mader M, Schlatter O, Heck B, Warmbold A, Dorn A, Zappe H, Risch P, Helmer D, Kotz F, Rapp BE (2021) High-throughput injection molding of transparent fused silica glass. *Science* 372(6538):182–186. <https://doi.org/10.1126/science.abf1537>
9. Chen X, Wang H, Zhang W (2020) Dynamic characteristics of abrasive grains and machined surface features for variable axis diamond grinding of quartz glass. *J Braz Soc Mech Sci Eng* 42:1–15. <https://doi.org/10.1007/s40430-020-02473-5>
10. Choi JH, Yoon J, Jung Y, Min KW, Im WB, Kim H (2021) Analysis of plasma etching resistance for commercial quartz glasses used in semiconductor apparatus in fluorocarbon plasma. *Mater Chem Phys* 272:125015. <https://doi.org/10.1016/j.mchemphys.2021.125015>
11. Khooshehmehri A, Eslami MA, Hosseini SA (2022) Design and fabrication of hemispherical shell resonator by glass blowing method. *J Electr Comput Eng Innov* 10(1):37–46. <https://doi.org/10.22061/JECEI.2021.7759.429>
12. Yang Z, Shan J, Huang Y, Dong X, Zheng W, Jin Y, Zhou W (2021) Preparation and mechanism of free-radical/cationic hybrid photosensitive resin with high tensile strength for three-dimensional printing applications. *J Appl Polym Sci* 138(8):49881. <https://doi.org/10.1002/app.49881>
13. Kotz F, Arnold K, Bauer W, Schild D, Keller N, Sachsenheimer K, Nargang TM, Richter C, Helmer D, Rapp BE (2017) Three-dimensional printing of transparent fused silica glass. *Nature* 544(7650):337–339. <https://doi.org/10.1038/nature22061>
14. Terpiłowski K, Wiśniewska M, Zarko VI (2015) Influence of solution pH, supporting electrolyte presence and solid content on the stability of aqueous nanosilica suspension. *J Ind Eng Chem* 30:71–76. <https://doi.org/10.1016/j.jiec.2015.05.003>
15. Zhang Q, Hu Y, Feng Y, Sun X, Duan J (2023) Critical role of water in fused silica glass by silica nanopowder sintering: Nanoparticle dispersion. *J Non-Cryst Solids* 609:122288. <https://doi.org/10.1016/j.jnoncrysol.2023.122288>
16. Chatterjee VA, Dey P, Verma SK, Bhattacharjee D, Biswas I, Neogi S (2019) Probing the intensity of dilatancy of high-performance shear-thickening fluids comprising silica in polyethylene glycol. *Mater Res Express* 6(7):075702. <https://doi.org/10.1088/2053-1591/ab1185>
17. Chen X, Huang Y, Zhang L, Liu J, Wang C, Wu M (2022) Cellulose nanofiber assisted dispersion of hydrophobic SiO₂ nanoparticles in water and its superhydrophobic coating. *Carbohydr Polym* 290:119504. <https://doi.org/10.1016/j.carbpol.2022.119504>
18. Tian S, Gao W, Liu Y, Kang W, Yang H (2020) Effects of surface modification Nano-SiO₂ and its combination with surfactant on interfacial tension and emulsion stability. *Colloid Surf A-Physicochem Eng Asp* 595:124682. <https://doi.org/10.1016/j.colsurfa.2020.124682>
19. Yuan J, Liu L, Wang X, Xu L, Zhang L (2022) Structure and performance of silica-Grafted epoxidized solution-polymerized

- styrene-butadiene nanocomposites. *Ind Eng Chem Res* 61(8):3031–3043. <https://doi.org/10.1021/acs.iecr.1c03702>
20. Hu C, Chen Y, Huang X, Liu H (2021) Effect of monofunctional monomers on rheological and photosensitive properties of resin-based alumina slurry for stereolithography. *Rare Met Mat Eng* 50(5):1576–1582
 21. Liu X, Yin J, Cheng W, Bu W, Fan Y, Wu Z (2011) Research on interface and fractal characteristics of PI/Al₂O₃ films by SAXS. *Acta Phys Sin* 60(5):173714. <https://doi.org/10.7498/aps.60.056101>
 22. Kamiya H, Fukuda Y, Suzuki Y, Tsukada M, Kakui T, Naito M (1999) Effect of polymer dispersant structure on electrosteric interaction and dense alumina suspension behavior. *J Am Ceram Soc* 82(2):3407–3412. <https://doi.org/10.1111/j.1151-2916.1999.tb02258.x>
 23. Zhao H, Dong B, Guo M (2004) Determination of the transition-layer thickness of a crystalline polymer by using small-angle X-ray scattering. *Acta Phys Sin* 53:1247–1250
 24. Whitby CP, Krebsz M, Booty SJ (2018) Understanding the role of hydrogen bonding in the aggregation of fumed silica particles in triglyceride solvents. *J Colloid Interface Sci* 527:1–9. <https://doi.org/10.1016/j.jcis.2018.05.029>
 25. Brown E, Jaeger HM (2014) Shear thickening in concentrated suspensions: phenomenology, mechanisms and relations to jamming. *Rep Prog Phys* 77(4):046602. <https://doi.org/10.1088/0034-4885/77/4/046602>
 26. Brown E, Zhang H, Forman NA, Maynor BW, Betts DE, DeSimone JM, Jaeger HM (2010) Shear thickening in densely packed suspensions of spheres and rods confined to few layers. *J Rheol* 54(5):1023–1046. <https://doi.org/10.1122/1.3474580>
 27. Ueno K, Imaizumi S, Hata K, Watanabe M (2009) Colloidal interaction in ionic liquids: effects of ionic structures and surface chemistry on rheology of silica colloidal dispersions. *Langmuir* 25(2):825–831. <https://doi.org/10.1021/la803124m>
 28. Nsib F, Ayed N, Chevalier Y (2007) Comparative study of the dispersion of three oxide pigments with sodium polymethacrylate dispersants in alkaline medium. *Prog Org Coat* 60(4):267–280. <https://doi.org/10.1016/j.porgcoat.2007.07.021>
 29. Sato Y, Hayami R, Gunji T (2022) Characterization of NMR, IR, and Raman spectra for siloxanes and silsesquioxanes: a mini review. *J Sol-Gel Sci Technol* 104(1):36–52. <https://doi.org/10.1007/s10971-022-05920-y>
 30. Warring SL, Beattie DA, McQuillan AJ (2016) Surficial siloxane-to-silanol interconversion during room-temperature hydration/dehydration of amorphous silica films observed by ATR-IR and TIR-Raman spectroscopy. *Langmuir* 32:1568–1576. <https://doi.org/10.1021/acs.langmuir.5b04506>
 31. Yamamoto K, Amaike Y, Tani M, Saito I, Kozuma T, Kaneko Y, Gunji T (2022) Bridged organosilica membranes incorporating carboxyl-functionalized cage silsesquioxanes for water desalination. *J Sol-Gel Sci Technol* 101(2):315–322. <https://doi.org/10.1007/s10971-021-05703-x>
 32. Hayami R, Ideno Y, Sato Y, Tsukagoshi H, Yamamoto K, Gunji T (2020) Soluble ethane-bridged silsesquioxane polymer by hydrolysis–condensation of bis (trimethoxysilyl) ethane: characterization and mixing in organic polymers. *J Polym Res* 27:1–10. <https://doi.org/10.1007/s10965-020-02294-z>
 33. Sato Y, Hayami R, Miyase Y, Ideno Y, Yamamoto K, Gunji T (2020) Preparation and properties of methyl- and cyclohexyl silsesquioxane oligomers as organic–inorganic filler. *J Sol-Gel Sci Technol* 95:474–481. <https://doi.org/10.1007/s10971-020-05291-2>
 34. Manorama SV, Reddy KM, Reddy CVG, Narayanan S, Raja PR, Chatterji PR (2002) Photostabilization of dye on anatase titania nanoparticles by polymer capping. *J Phys Chem Solids* 63(1):135–143. [https://doi.org/10.1016/S0022-3697\(01\)00089-0](https://doi.org/10.1016/S0022-3697(01)00089-0)
 35. Wang YJ, Zhang XN, Song Y, Zhao Y, Chen L, Su F, Li L, Wu Z, Zheng Q (2019) Ultrastiff and tough supramolecular hydrogels with a dense and robust hydrogen bond network. *Chem Mater* 31(4):1430–1440. <https://doi.org/10.1021/acs.chemmater.8b05262>
 36. Plotnichenko VG, Sokolov VO, Dianov EM (2000) Hydroxyl groups in high-purity silica glass. *J Non-Cryst Solids* 36:404–410
 37. Kawaguchi M (2020) Stability and rheological properties of silica suspensions in water-immiscible liquids. *Adv Colloid Interface Sci* 278:102139. <https://doi.org/10.1016/j.cis.2020.102139>
 38. Mu Y, Chen J, An X, Liang J, Li J, Zhou Y, Sun X (2023) Effect of synergism of solid loading and sintering temperature on microstructural evolution and mechanical properties of 60 vol% high solid loading ceramic core obtained through stereolithography 3D printing. *J Eur Ceram Soc* 43(2):661–675. <https://doi.org/10.1016/j.jeurceramsoc.2022.10.051>
 39. Kim KD, Lee SH, Ahn HK (2004) Observation of nucleation effect on crystallization in lithium aluminosilicate glass by viscosity measurement. *J Non-Cryst Solids* 336(3):195–201. <https://doi.org/10.1016/j.jnoncrysol.2004.01.001>
 40. Wang LY, Hon MH (1995) The effect of cristobalite seed on the crystallization of fused silica based ceramic core—a kinetic study. *Ceram Int* 21(3):187–193. [https://doi.org/10.1016/0272-8842\(95\)90909-3](https://doi.org/10.1016/0272-8842(95)90909-3)
 41. Raghavan SR, Walls HJ, Khan SA (2000) Rheology of silica dispersions in organic liquids: new evidence for solvation forces dictated by hydrogen bonding. *Langmuir* 16(21):7920–7930. <https://doi.org/10.1021/la991548q>
 42. Zhang Q, Hu Y, Duan J, Feng Y, Chen H, Zheng H, Sun X (2024) Dispersion of silica nanoparticles in water/ethanol/PEG mixtures for stimuli-responsive aggregation to prepare improved fused silica glass. *Ceram Int* 50(1):2340–2349. <https://doi.org/10.1016/j.ceramint.2023.11.012>

Publisher's note Springer Nature remains neutral with regard to jurisdictional claims in published maps and institutional affiliations.

Springer Nature or its licensor (e.g. a society or other partner) holds exclusive rights to this article under a publishing agreement with the author(s) or other rightsholder(s); author self-archiving of the accepted manuscript version of this article is solely governed by the terms of such publishing agreement and applicable law.